

Results of the Ultra-Heavy Cosmic-Ray Analysis with CALET on the International Space Station

Wolfgang V. Zober^{a,*} and Brian F. Rauch^a for the CALET collaboration

^aDepartment of Physics and McDonnell Center for the Space Sciences, Washington University,
St. Louis, MO 63130 USA

E-mail: wzober@wustl.edu

The CALorimetric Electron Telescope (CALET), launched to the ISS in August 2015 and in continuous operation since, measures cosmic-ray (CR) electrons, nuclei, and gamma rays. CALET, with its 27 radiation length deep Total Absorption Calorimeter (TASC), measures particle energy, allowing for the determination of spectra and secondary to primary ratios of the more abundant CR nuclei through ^{28}Ni , while the main charge detector (CHD) can measure Ultra-Heavy (UH) CR nuclei through ^{40}Zr . Previous CALET UHGCR analyses used a special high duty cycle ($\sim 90\%$) UH trigger that does not require passage through the TASC and used time- and position-dependent detector response corrections based on ^{14}Si and ^{26}Fe and an angle-dependent geomagnetic cutoff rigidity selection to show abundances of even nuclei in agreement with SuperTIGER and ACE-CRIS. The work shown here further improves upon those results by restricting UH events to those that pass through both the TASC and CHD. While this constraint does reduce the number of events to $\sim 1/6$ of the original UH trigger analysis, the loss of statistics is compensated by improvements in event selection from an energy-binned charge determination and minimum deposited energy that substitutes for the previous minimum geomagnetic rigidity selection. The results shown here represent 7 years of observation for the abundances of elements from $Z=10$ to $Z=40$ relative to ^{26}Fe and are compared to previous measurements from ACE-CRIS, SuperTIGER, and HEAO-3.

38th International Cosmic Ray Conference (ICRC2023)
26 July - 3 August, 2023
Nagoya, Japan



*Speaker

1. Introduction

The CALorimetric Electron Telescope (CALET) on the International Space Station (ISS) is a Japanese led astroparticle observatory that was launched on August 19, 2015 and has been collecting scientific data since October 13, 2015. As its name suggests, the main science objective of CALET is to directly measure the total cosmic-ray electron flux ($e^- + e^+$) to the highest energies (1 GeV to 20 TeV) with the main calorimeter (CAL), shown in the CALET instrument package in Fig. 1a. The calorimeter is also capable of measuring gamma rays (10 GeV to 10 TeV) and cosmic-ray nuclei (up to 1,000 TeV). In addition, there is the CALET Gamma-ray Burst Monitor (CGBM), which can make simultaneous observations with the calorimeter [1].

CAL is comprised of three detector systems, shown in more detail in Figs. 1a and 1b. At the top of CALET is the charge detector (CHD), which is comprised of an x and a y layer, each layer having 14 scintillator paddles. These paddles all are 32 mm wide by 10 mm thick by 450 mm long. Right below the CHD is the imaging calorimeter (IMC), which is 156.5 mm tall, and made of 8 layers of both x and y scintillating fibers that are 1 mm wide squares and 448 mm long. In between the fiber layers of the IMC are a combined 3.0 radiation lengths (X_0) of tungsten arranged such that the first 5 layers are $0.2X_0$ thick and the bottom two are each $1.0X_0$ thick. At the bottom of the instrument stack is the total absorption calorimeter (TASC). The TASC is made of 6 x and y layers of 16 lead tungstate (PWO) scintillator logs. Each of these logs are 19 mm wide, 20 mm tall, and 326 mm long. Combined these logs give the TASC a total depth of $27X_0$.

The CHD, along with the IMC, together provides the primary particle charge identification. All three detectors are utilized for track reconstruction, but that is primarily based on the IMC, while the particle energy is determined from the calorimeters, with most of the determination based on TASC measurements.

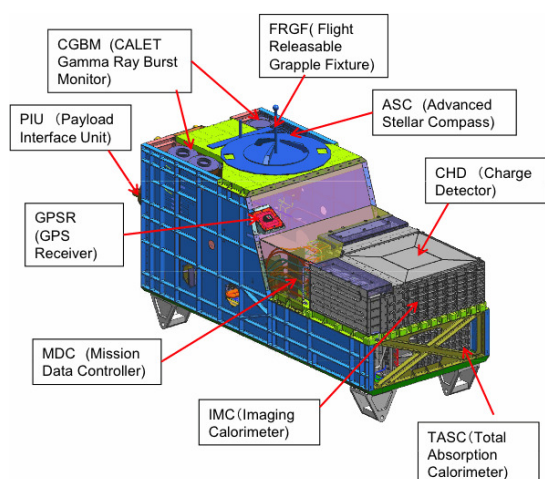


Figure 1(a): CALET instrument package detailing locations of the various CALET subsystems.

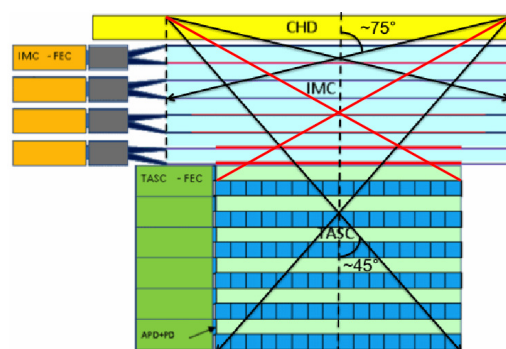


Figure 1(b): CALET side-view showing CHD, IMC, and TASC detector placement with the maximum acceptance angles for detection. The maximum acceptance angle (75°) for the UH trigger analysis is shown in black and in red for the TASC analysis (45°).

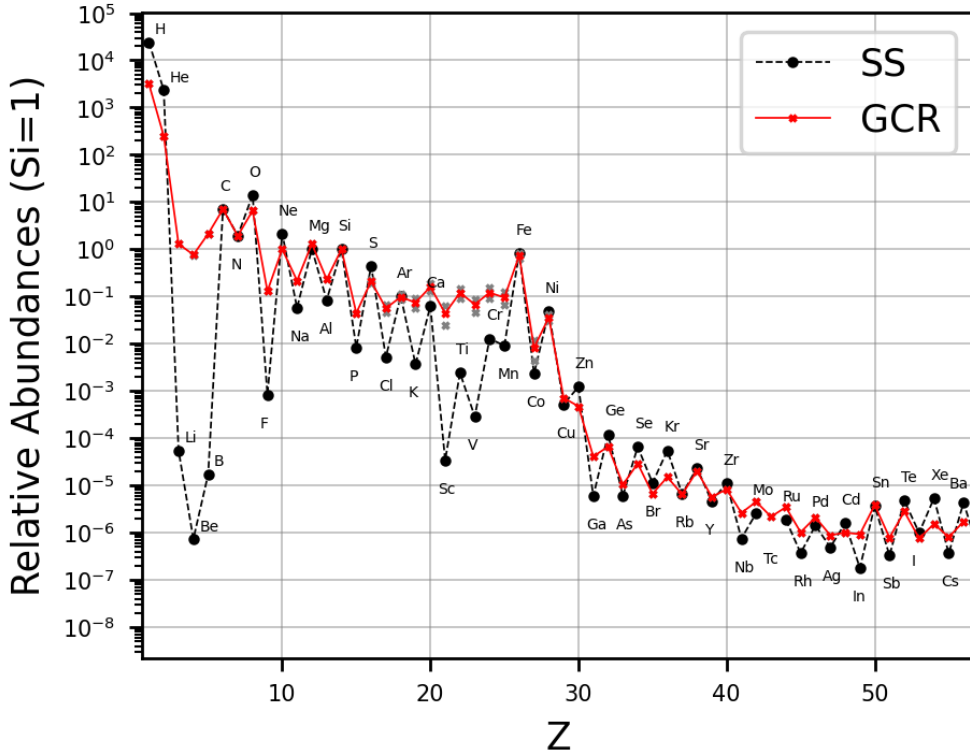


Figure 2: Solar System (SS) [2] and Galactic cosmic-ray (GCR) relative abundances at 2 GeV/nuc. The red line depicts average GCR data, sourced for $1 \leq Z \leq 2$ from [3], $Z=3$ from [4], $4 \leq Z \leq 28$ from [5], and $16 \leq Z \leq 56$ from [6] normalized to ${}_{14}\text{Si}$. Grey dots depict overlapping measurements from [5] and [6].

2. Ultra-Heavy Cosmic Rays

The measurement of ultra-heavy Galactic cosmic rays (UHGCR), ${}_{30}\text{Zn}$ and higher charge elements, provides insight into the origins of cosmic rays. In Fig. 2, the relative abundances of cosmic rays elements ($1 \leq Z \leq 56$) with energies of 2 GeV/nucleon are compared to the Solar System (SS) abundances normalized to ${}_{14}\text{Si}$ [2–6]. These two samples of Galactic matter are nominally consistent, with most of the differences accounted for by cosmic ray spallation between source and detection and by acceleration efficiencies. In the cosmic rays we see that ${}_{26}\text{Fe}$ is $\sim 5 \times 10^3$ times less abundant than ${}_{1}\text{H}$, and that the UHGCR with charges $30 \leq Z \leq 40$ are $\sim 10^5$ times less abundant than ${}_{26}\text{Fe}$. Single-element resolution UHGCR measurements have so far only been made by a small number of instruments. For balloon-borne measurements these go up to ${}_{40}\text{Zr}$ by TIGER [7] and up to ${}_{56}\text{Ba}$ by SuperTIGER [8] at $\sim \text{GeV/nuc}$ energies, while the single element space based measurements only go up to ${}_{38}\text{Zr}$ by the ACE-CRIS [14] instrument at hundreds of MeV/nuc.

These experiments find that UHGCR composition shows enhancement in material produced in massive stars, both from stellar outflows during the stars' lives and in the ejecta from supernovae. This suggests that a significant fraction of the cosmic rays may originate in OB associations, which is where the majority of supernovae that are believed to accelerate the Galactic cosmic rays occur. The fact that the cosmic-ray source appears to be enhanced in massive star material compared to SS would suggest that UHGCR observations can help constrain the relative contributions of supernovae

and binary neutron star mergers to the heavy r-process elements.

Our CALET observations contribute to the statistics of the UHGCR data set and complement other existing measurements. The ultra-heavy (UH) event trigger on CALET, which requires events only pass through the CHD and top half of the IMC, has collected UHGCR statistics similar to those achieved in the first flight of the balloon-borne SuperTIGER instrument. CALET also observes a similar energy range to TIGER and SuperTIGER, but requires corrections for different systematic effects. The balloon-based observations must be corrected for energy losses and nuclear interactions that occur in the atmosphere, while ISS based measurements are only subject to screening by Earth's geomagnetic field. Comparatively, UHGCR observations made by ACE-CRIS occur outside the geomagnetic field in a complementary lower energy range. So while the ACE-CRIS and SuperTIGER instruments only measure down to ${}^5\text{B}$ and ${}^{10}\text{Ne}$, respectively, CALET's measurements of cosmic-ray abundances in the $13 \leq Z \leq 44$ charge range provide complementary measurements and a check of the cross calibrations of other instruments.

3. Data, corrections, and screens

As stated above, the UH trigger requires events only pass through the CHD and top half of the IMC. If one chooses to perform analysis on the full UH trigger dataset one needs to use the minimum geomagnetic cutoff as a proxy for energy. This method was shown at the previous ICRC in [10]. Here we explore usage of a subset of UH trigger data that requires particles to pass through part of the TASC. As with the previous analysis, we need to perform some minor secondary corrections on the data set.

The CALET instrument already has a number of corrections applied to the dataset, however these corrections are optimized for the main analysis, with corrections applied to all data based on helium and protons. Since the UH analysis events have significantly different detector signals, we need

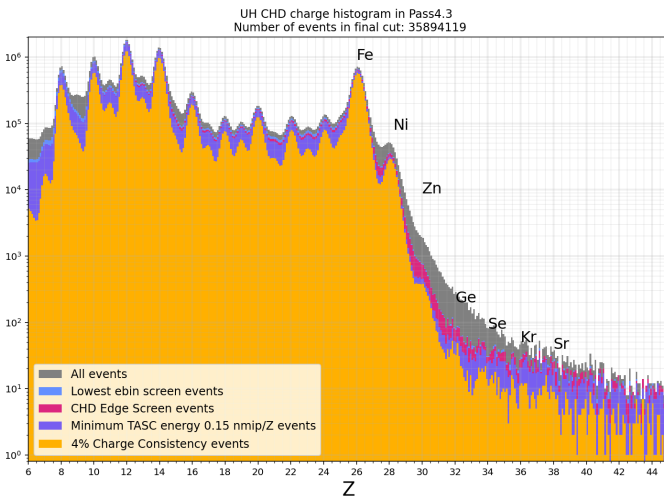


Figure 3: The TASC UH dataset, with successive screens applied. A minimum TASC Edep of 1.53 nmip to remove the lowest 3 energy bins, a screen on the event location, a minimum TASC Edep/Z, and the 4 percent charge consistency screen.

to perform our own set of secondary corrections to optimize the UH region. To do this we do corrections based on position and event date of detection.

The position corrections are derived by dividing each CHD paddle into 42 segments (with length $\sim 1/3$ of paddle width). For each individual paddle segment we perform a Gaussian fit on ${}^{26}\text{Fe}$ and ${}^{14}\text{Si}$ events to determine the local peak mean signal for those elements. We then take these local means and find the ratio of the full layer means for both ${}^{26}\text{Fe}$ and ${}^{14}\text{Si}$ respectively. We then plug these ratios into a function to smoothly transition between those correction factors allowing for a seamless correction that can be applied to all UH

events. The time corrections are performed similarly, with the "local" segments being defined as increments in time where there are a minimum 550 events in each paddle. This results in time correction bins being approximately 3 days in length.

Since the last ICRC, work has continued on the analysis of the subset of events that pass through the TASC within the 45° acceptance angle shown in Fig. 1b, which provides each event with energy information. The TASC energy measurement comes in the form of deposited energy as a function of number of minimum ionizing particles (nmip). While this value is not an exact energy, as that requires a deconvolution of TASC energy responses every event, it does suffice as a value that allows for separation of events into groups of energy. After the grouping of events by deposited energy we perform a Tarle model charge assignment [9] on each deposited energy bin, and remerge the bins.

After all corrections are performed, we perform a number of event selection screens. In the analysis shown here we perform cuts for an overall minimum deposited energy and the deposited energy by charge. These two cuts are applied to remove low energy events that cause a smearing of charge. Additionally, we apply a charge consistency cut requiring that the calculated CHD charge for both x and y layers is within 4% to remove interacting events. Finally, we apply a screen on position, removing the events closest to the edge of CHD, and a screen on time to account for a few bad time bins where the ISS displayed abnormal behavior.

The successive effects of these cuts are shown in Fig. 3. For further details on how all of these corrections have been implemented and on how each screen is determined please see [11].

4. Determination of Abundances

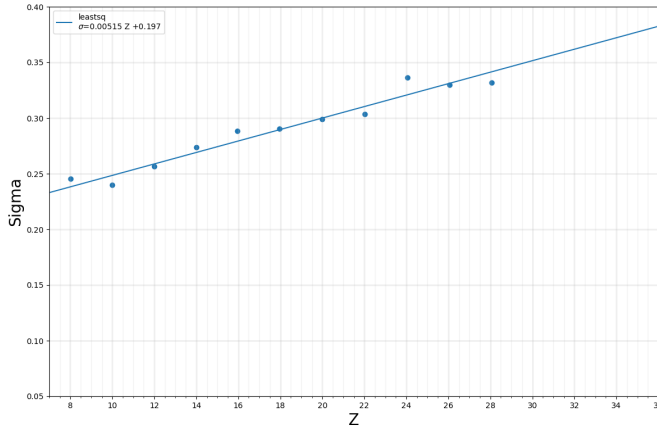


Figure 4: Linear fit on the sigmas from the initial fit. Successive fits are required to have peak width be within 2 percent of the best fit function shown here.

In the second iteration of the multigaussian we add the constraint that all peak sigmas must be within 2% of the linear best fit. From this second fit we record the final sigmas and peak positions. After this is the third and final fit, where only peak amplitudes are allowed to vary. The results of this fit are shown in Fig. 5.

To determine the total error on the fit we combine three error sources in quadrature. First, is the error returned from the fit itself, second is the statistical error derived by Gehrels [12], and finally a

To find abundances for the UH analysis we use a similar methodology to one originally implemented in the SuperTIGER analysis [6]. This methodology has us perform multiple iterations of a maximum-likelihood Gaussian fits that add in constraints based on prior fit information. The first iteration of the fit is applied to all $Z \leq 50$ with the only constraint being full integer spacing between all peaks. From this fit we take the peak widths of all even peaks and perform the linear fit shown in Fig. 4 on the even elements in $8 \leq Z \leq 28$. In the

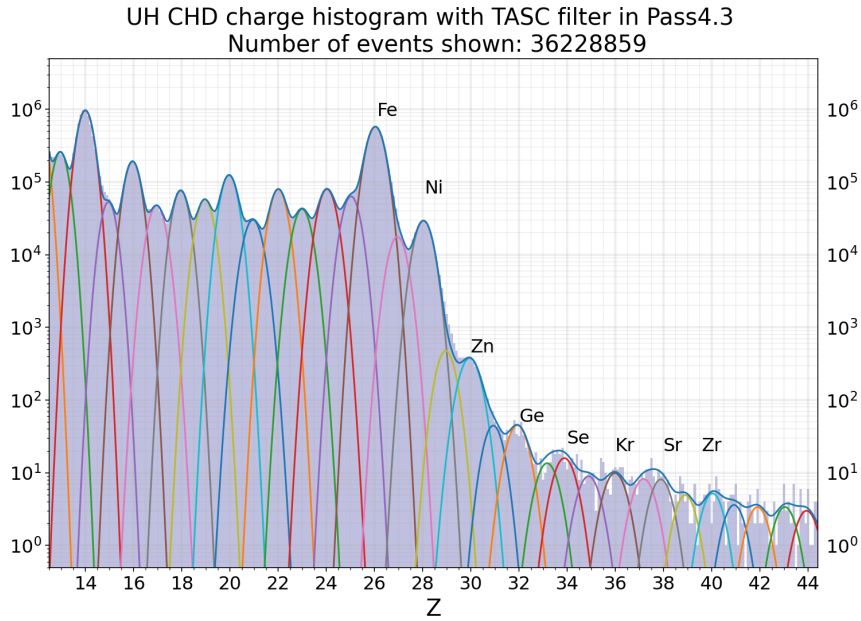


Figure 5: Here we show the results of the multigaussian fit procedure for the TASC UH abundances. The number of events within the full fit is roughly identical to the number in the histogram (<1% difference between fit and histogram in the UH region)

variational error derived from the choice in screens is used. To get this third error source, we repeat the final step in the fitting routine on a set of alternative histograms. Some of these histograms are shown in Fig 6a and possess slightly different screens: a change in minimum Edep/Z and/or maximum percent difference. We take the results of each fit and take the difference in abundances between the alternative and original histogram in Figure 5. We use the maximum differences in positive and negative relative abundances as the error.

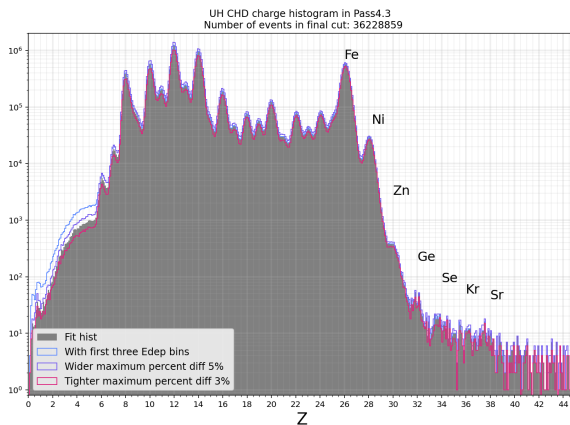


Figure 6(a): Example histograms for derivation of variational error. The histograms above explore differences in the Edep screen and changes in the percent difference between CHDX and CHDY.

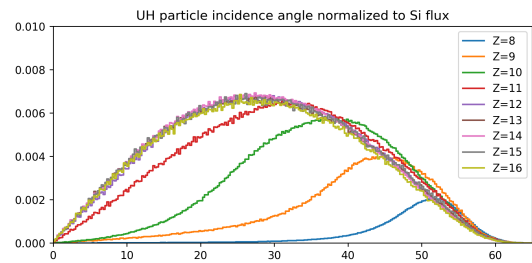


Figure 6(b): Incidence event angle with a weighted normalization to the ^{14}Si flux to show minimum acceptance angle changes with Z. 0° is vertical entry and bin size is 0.25° .

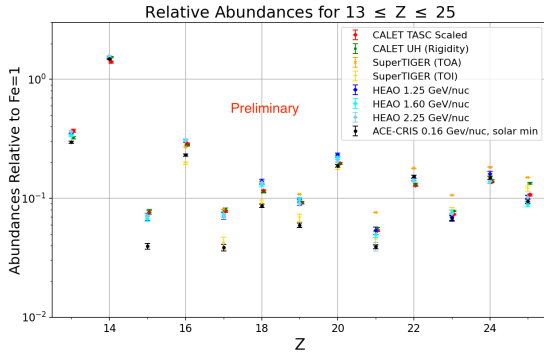


Figure 7(a): Abundances for $Z < 26$ compared to abundances from HEAO-3-C2 for 1.25 to 2.25 GeV/nuc [5], ACE-CRIS [13], and both SuperTIGER top of instrument [8] and top of atmosphere [6]. The CALET UH abundances derived via a rigidity cutoff is in red.

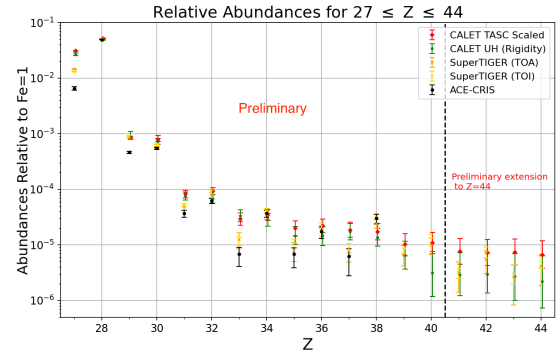


Figure 7(b): CALET UH Abundances for $Z > 26$ compared to the abundances from ACE-CRIS [14] and both SuperTIGER top of instrument [8] and top of atmosphere [6]. The CALET UH abundances derived via a rigidity cutoff is in red.

After this we also correct the abundances for low Z by comparing and if needed normalizing lower Z peaks to the angular event distribution of ^{14}Si . This is to account for systematic effects caused by the UH trigger, as low Z events only trigger at shallower angles. By exploring how event count for Z changes with incident angle in Fig 6b, we can rescale low Z peaks to what they may have been without the UH trigger bias.

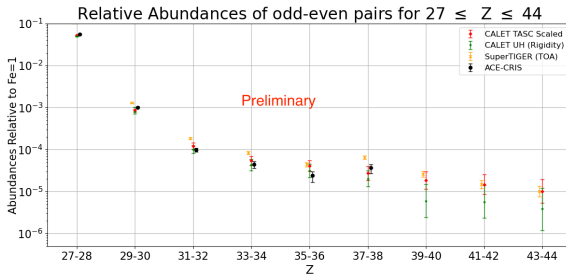


Figure 8: The relative abundances of the Odd-Even element pairs compared to abundances from ACE-CRIS [14] and SuperTIGER. [6] The CALET UH abundances derived via a rigidity cutoff is in red.

In these plots we can see good consistency between the space-based measurements and CALET. We note that there are some minor differences from SuperTIGER, but these may be caused by problems with the atmospheric corrections. The current work done in [15] shows a revised atmospheric correction that may bring SuperTIGER's results to be in line with CALET.

5. Conclusions

Abundances from CALET UH-trigger and TASC UHGCR analyses continue to agree with previous CALET results and other instrument measurements. After 7.5 years, CALET continues to output excellent data, and it is expected to continue operating for several more years. This further

data-collection will allow improved statistics for CALET to contribute to the total UHGCR data set, and complement the measurements made by other balloon and space-borne instruments.

Acknowledgements

We gratefully acknowledge JAXA's contributions to the development of CALET and to the operations onboard the International Space Station. The CALET effort in Italy is supported by ASI under Agreement No. 2013-018-R.0 and its amendments. The CALET effort in the United States is supported by NASA through Grants No. 80NSSC20K0397, No. 80NSSC20K0399, and No. NNH18ZDA001N-APRA18-0004. This work is supported in part by JSPS Grant-in-Aid for Scientific Research (S) Grant No. 19H05608 in Japan.

The material contained in this document is based upon work supported by a National Aeronautics and Space Administration (NASA) grant or cooperative agreement. Any opinions, findings, conclusions, or recommendations expressed in this material are those of the author and do not necessarily reflect the views of NASA.

References

- [1] S. Torii et al. (CALET Collaboration), *Highlights from the CALET observations for 7.5 years on the International Space Station*, in proceedings of *The 38th International Cosmic Ray Conference*, 2023
- [2] K. Lodders, Solar System Abundances and Condensation Temperatures of the Elements, *ApJ*, 591(2003) 1220-1247.
- [3] T. Sanuki et al., Precise Measurement of Cosmic-Ray Proton and Helium Spectra with the BESS Spectrometer, *ApJ*, 545(2000) 148-155, [arXiv:astro-ph/0002481](https://arxiv.org/abs/astro-ph/0002481).
- [4] M. Aguilar et al., Isotopic Composition of Light Nuclei in Cosmic Rays: Results from AMS-01, *ApJ*, 736(2011), 105-116, [arXiv:1106.2269](https://arxiv.org/abs/1106.2269)
- [5] J.J. Engelmann et al., Charge composition and energy spectra of cosmic-ray nuclei for elements from Be to Ni - Results from HEAO-3-C2, *A&A*, 233(1990), 96-111
- [6] N. Walsh, *SuperTiger Elemental Abundances for the Charge Range $41 \leq Z \leq 56$* , Doctoral dissertation, Washington University in St. Louis, 2020
- [7] B.F. Rauch et al., *Cosmic Ray origin in OB Associations and Preferential Acceleration of Refractory Elements: Evidence from Abundances of Elements $_{26}\text{Fe}$ through $_{34}\text{Se}$* , *ApJ*, 697(2009) 2083-2088, [arXiv:0906.2021](https://arxiv.org/abs/0906.2021)
- [8] N. Walsh et al., *SuperTIGER instrument abundances of Galactic cosmic rays for the charge interval $41 \leq Z \leq 56$* , *Advances in Space Research*, Volume 70, Issue 9, 2022. [DOI](https://doi.org/10.1016/j.asr.2022.09.011)
- [9] G. Tarle, S. P. Ahlen, and B. G. Cartwright. *Cosmic Ray Isotope Abundances from Chromium to Nickel*. *ApJ*, 230(1979), 607–620.
- [10] W.V. Zober et al. (CALET Collaboration), *Progress on Ultra-Heavy Cosmic-Ray Analysis with CALET on the International Space Station* in proceedings of *The 37th International Cosmic Ray Conference*, 2021
- [11] W.V. Zober et al. (CALET Collaboration), *Optimizing Selection Criteria for the CALET Ultra-Heavy Cosmic Ray Analysis*, in proceedings of *The 38th International Cosmic Ray Conference*, 2023
- [12] N. Gehrels, *Confidence Limits for Small Numbers of Events in Astrophysical Data*, 1985 *ApJ* 303.
- [13] M. H. Israel et al. *Elemental Composition at the Cosmic-Ray Source Derived from the ACE-CRIS Instrument. I. $_{6}\text{C}$ to $_{28}\text{Ni}$* 2018 *ApJ* 865 69
- [14] W.R. Binns et al., *The Isotopic Abundances of Galactic Cosmic Rays with Atomic Number $29 \leq Z \leq 38$* , *ApJ* 936 13.
- [15] N. Osborne et al., *SuperTIGER Atmospheric Corrections and Uncertainty Analysis*, in proceedings of *The 38th International Cosmic Ray Conference*, 2023

Full Author List: CALET Collaboration

O. Adriani^{1,2}, Y. Akaike^{3,4}, K. Asano⁵, Y. Asaoka⁵, E. Berti^{2,6}, G. Bigongiari^{7,8}, W.R. Binns⁹, M. Bongi^{1,2}, P. Brogi^{7,8}, A. Bruno¹⁰, N. Cannady^{11,12,13}, G. Castellini⁶, C. Checchia^{7,8}, M.L. Cherry¹⁴, G. Collazuol^{15,16}, G.A. de Nolfo¹⁰, K. Ebisawa¹⁷, A.W. Ficklin¹⁴, H. Fuke¹⁷, S. Gonzi^{1,2,6}, T.G. Guzik¹⁴, T. Hams¹¹, K. Hibino¹⁸, M. Ichimura¹⁹, K. Ioka²⁰, W. Ishizaki⁵, M.H. Israel⁹, K. Kasahara²¹, J. Kataoka²², R. Kataoka²³, Y. Katayose²⁴, C. Kato²⁵, N. Kawanaka²⁰, Y. Kawakubo¹⁴, K. Kobayashi^{3,4}, K. Kohri²⁶, H.S. Krawczynski⁹, J.F. Krizmanic¹², P. Maestro^{7,8}, P.S. Marrocchesi^{7,8}, A.M. Messineo^{8,27}, J.W. Mitchell¹², S. Miyake²⁸, A.A. Moiseev^{29,12,13}, M. Mori³⁰, N. Mori², H.M. Motz¹⁸, K. Munakata²⁵, S. Nakahira¹⁷, J. Nishimura¹⁷, S. Okuno¹⁸, J.F. Ormes³¹, S. Ozawa³², L. Pacini^{2,6}, P. Papini², B.F. Rauch⁹, S.B. Ricciarini^{2,6}, K. Sakai^{11,12,13}, T. Sakamoto³³, M. Sasaki^{29,12,13}, Y. Shimizu¹⁸, A. Shiomi³⁴, P. Spillantini¹, F. Stolzi^{7,8}, S. Sugita³³, A. Sulaj^{7,8}, M. Takita⁵, T. Tamura¹⁸, T. Terasawa⁵, S. Torii³, Y. Tsunesada^{35,36}, Y. Uchihori³⁷, E. Vannuccini², J.P. Wefel¹⁴, K. Yamaoka³⁸, S. Yanagita³⁹, A. Yoshida³³, K. Yoshida²¹, and W.V. Zober⁹

¹Department of Physics, University of Florence, Via Sansone, 1 - 50019, Sesto Fiorentino, Italy, ²INFN Sezione di Firenze, Via Sansone, 1 - 50019, Sesto Fiorentino, Italy, ³Waseda Research Institute for Science and Engineering, Waseda University, 17 Kikuicho, Shinjuku, Tokyo 162-0044, Japan, ⁴JEM Utilization Center, Human Spaceflight Technology Directorate, Japan Aerospace Exploration Agency, 2-1-1 Sengen, Tsukuba, Ibaraki 305-8505, Japan, ⁵Institute for Cosmic Ray Research, The University of Tokyo, 5-1-5 Kashiwa-no-Ha, Kashiwa, Chiba 277-8582, Japan, ⁶Institute of Applied Physics (IFAC), National Research Council (CNR), Via Madonna del Piano, 10, 50019, Sesto Fiorentino, Italy, ⁷Department of Physical Sciences, Earth and Environment, University of Siena, via Roma 56, 53100 Siena, Italy, ⁸INFN Sezione di Pisa, Polo Fibonacci, Largo B. Pontecorvo, 3 - 56127 Pisa, Italy, ⁹Department of Physics and McDonnell Center for the Space Sciences, Washington University, One Brookings Drive, St. Louis, Missouri 63130-4899, USA, ¹⁰Heliospheric Physics Laboratory, NASA/GSFC, Greenbelt, Maryland 20771, USA, ¹¹Center for Space Sciences and Technology, University of Maryland, Baltimore County, 1000 Hilltop Circle, Baltimore, Maryland 21250, USA, ¹²Astroparticle Physics Laboratory, NASA/GSFC, Greenbelt, Maryland 20771, USA, ¹³Center for Research and Exploration in Space Sciences and Technology, NASA/GSFC, Greenbelt, Maryland 20771, USA, ¹⁴Department of Physics and Astronomy, Louisiana State University, 202 Nicholson Hall, Baton Rouge, Louisiana 70803, USA, ¹⁵Department of Physics and Astronomy, University of Padova, Via Marzolo, 8, 35131 Padova, Italy, ¹⁶INFN Sezione di Padova, Via Marzolo, 8, 35131 Padova, Italy, ¹⁷Institute of Space and Astronautical Science, Japan Aerospace Exploration Agency, 3-1-1 Yoshinodai, Chuo, Sagamihara, Kanagawa 252-5210, Japan, ¹⁸Kanagawa University, 3-27-1 Rokkakubashi, Kanagawa, Yokohama, Kanagawa 221-8686, Japan, ¹⁹Faculty of Science and Technology, Graduate School of Science and Technology, Hirosaki University, 3, Bunkyo, Hirosaki, Aomori 036-8561, Japan, ²⁰Yukawa Institute for Theoretical Physics, Kyoto University, Kitashirakawa Oiwake-cho, Sakyo-ku, Kyoto, 606-8502, Japan, ²¹Department of Electronic Information Systems, Shibaura Institute of Technology, 307 Fukasaku, Minuma, Saitama 337-8570, Japan, ²²School of Advanced Science and Engineering, Waseda University, 3-4-1 Okubo, Shinjuku, Tokyo 169-8555, Japan, ²³National Institute of Polar Research, 10-3, Midori-cho, Tachikawa, Tokyo 190-8518, Japan, ²⁴Faculty of Engineering, Division of Intelligent Systems Engineering, Yokohama National University, 79-5 Tokiwadai, Hodogaya, Yokohama 240-8501, Japan, ²⁵Faculty of Science, Shinshu University, 3-1-1 Asahi, Matsumoto, Nagano 390-8621, Japan, ²⁶Institute of Particle and Nuclear Studies, High Energy Accelerator Research Organization, 1-1 Oho, Tsukuba, Ibaraki, 305-0801, Japan, ²⁷University of Pisa, Polo Fibonacci, Largo B. Pontecorvo, 3 - 56127 Pisa, Italy, ²⁸Department of Electrical and Electronic Systems Engineering, National Institute of Technology (KOSEN), Ibaraki College, 866 Nakane, Hitachinaka, Ibaraki 312-8508, Japan, ²⁹Department of Astronomy, University of Maryland, College Park, Maryland 20742, USA, ³⁰Department of Physical Sciences, College of Science and Engineering, Ritsumeikan University, Shiga 525-8577, Japan, ³¹Department of Physics and Astronomy, University of Denver, Physics Building, Room 211, 2112 East Wesley Avenue, Denver, Colorado 80208-6900, USA, ³²Quantum ICT Advanced Development Center, National Institute of Information and Communications Technology, 4-2-1 Nukui-Kitamachi, Koganei, Tokyo 184-8795, Japan, ³³College of Science and Engineering, Department of Physics and Mathematics, Aoyama Gakuin University, 5-10-1 Fuchinobe, Chuo, Sagamihara, Kanagawa 252-5258, Japan, ³⁴College of Industrial Technology, Nihon University, 1-2-1 Izumi, Narashino, Chiba 275-8575, Japan, ³⁵Graduate School of Science, Osaka Metropolitan University, Sugimoto, Sumiyoshi, Osaka 558-8585, Japan, ³⁶Nambu Yoichiro Institute for Theoretical and Experimental Physics, Osaka Metropolitan University, Sugimoto, Sumiyoshi, Osaka 558-8585, Japan, ³⁷National Institutes for Quantum and Radiation Science and Technology, 4-9-1 Anagawa, Inage, Chiba 263-8555, Japan, ³⁸Nagoya University, Furo, Chikusa, Nagoya 464-8601, Japan, ³⁹College of Science, Ibaraki University, 2-1-1 Bunkyo, Mito, Ibaraki 310-8512, Japan